212 *Chem. Mater.* **2010,** *22,* 212–217
DOI:10.1021/cm903099w

CHEMISTRY OF MATERIALS
Article

Iron Oxide-Based Nanotube Arrays Derived from Sacrificial Template-Accelerated Hydrolysis: Large-Area Design and Reversible Lithium Storage

Jinping Liu,*[,†,||] Yuanyuan Li,[‡,||] Hongjin Fan,[§] Zhihong Zhu,[†] Jian Jiang,[†] Ruimin Ding,[†] Yingying Hu,[†] and Xintang Huang*[,†]

[†]*Institute of Nanoscience and Nanotechnology, Department of Physics, Central China Normal University, Wuhan 430079, P. R. China,* [‡]*State Key Laboratory of Advanced Technology for Materials Synthesis and Processing, Wuhan University of Technology, Wuhan 430070, P. R. China, and* [§]*Division of Physics and Applied Physics, School of Physical and Mathematical Sciences, Nanyang Technological University, Singapore 637371.* [||] *These authors contribute equally to this work*

Received October 7, 2009. Revised Manuscript Received October 29, 2009

We report a novel "sacrificial template-accelerated hydrolysis" (STAH) approach to the synthesis of iron oxide-based nanotube arrays including hematite α-Fe_2O_3 and magnetite Fe_3O_4 on centimeter-scale conducting alloy substrates. ZnO nanowire arrays are chosen as the inexpensive and sacrificial templates that do not contribute to the component of final iron oxide nanotubes but can be in situ dissolved by the acid produced from the Fe^{3+} precursor hydrolysis. Interestingly, the ZnO template dissolution in turn accelerates the Fe^{3+} hydrolysis, which is essential to initiating the nanotube formation. Such a STAH approach provides a morphology-reservation transformation, when various shaped ZnO templates are adopted. Moreover, by introducing glucose into the precursor solution, we also successfully obtain carbon/hematite(C/α-Fe_2O_3) composite nanotube arrays on large-area flexible alloy substrate, with a large number of pores and uniform carbon distribution at a nanoscale in the nanotube walls. These arrays have been demonstrated as excellent additive-free anode materials for lithium ion batteries in terms of good cycling performance up to 150 times (659 mA h g^{-1}) and outstanding rate capability. Our result presents not only a new route for inorganic nanotube formation but also an insight for rational design of advanced electrode materials for electrochemical batteries and sensors.

1. Introduction

Inorganic nanotubes lie at the heart of one-dimensional nanostructures[1,2] and have attracted great scientific interest because of their unique physicochemical properties, which are directly related to their structural features such as the ultrahigh surface area, large porosity, and availability of a hollow cavity.[3−9] Nanotubes have application potentials in fluidic sensors, energy storage, and biomedicine. There are currently a number of synthetic strategies to inorganic tubular nanostructures including direct assembly, template-directed growth, electrochemical anodization, as reviewed previously.[10] Among them, templated synthesis[1,8,11−14] has been applied to a wide spectrum of nanotubes made from nonlayered materials such as GaN, silica, TiO_2, ZnS and metals. Early typical examples were the use of carbon nanotubes and porous membranes as removable templates to fabricate metal oxide hollow objects.[11,12] Recently, Fan et al.[15] reported ternary oxide nanotube synthesis such as $ZnAl_2O_4$ by the reaction between the metal oxide core "substrate" (template) and shell of a designed coaxial nanowire, based on the nanoscale Kirkendall effect. In most previous templating processes, an extra step involving thorough template removal (via heating/chemical treatments) was needed if none of the constitutional atoms of template were incorporated into the nanotubes;[1,14] in the case that the incorporation was present but not complete so that

*To whom correspondence should be addressed. Fax +86-027-67861185. E-mail: liujp@phy.ccnu.edu.cn (J.L.); xthuang@phy.ccnu.edu.cn (X.H.).

(1) Goldberger, J.; He, R. R.; Zhang, Y. F.; Lee, S. W.; Yan, H. Q.; Choi, H. J.; Yang, P. D. *Nature* **2003**, *422*, 599–602.
(2) Tenne, R. *Nat. Nanotechnol.* **2006**, *1*, 103–111.
(3) Hulteen, J. C.; Martin, C. R. *J. Mater. Chem.* **1997**, *7*, 1075–1087.
(4) Mor, G. K.; Shankar, K.; Paulose, M.; Varghese, O. K.; Grimes, C. A. *Nano Lett.* **2006**, *6*, 215–218.
(5) Nishizawa, M.; Menon, V. P.; Martin, C. R. *Science* **1995**, *268*, 700–702.
(6) (a) Lou, X. W.; Archer, L. A.; Yang, Z. C. *Adv. Mater.* **2008**, *20*, 3987–4019. (b) Zeng, H. B.; Cai, W. P.; Liu, P. S.; Xu, X. X.; Zhou, H. J.; Klingshirn, C.; Kalt, H. *ACS Nano* **2008**, *2*, 1661–1670.
(7) Hu, J.; Bando, Y.; Liu, Z.; Zhan, J.; Golberg, D.; Sekiguchi, T. *Angew. Chem., Int. Ed.* **2004**, *43*, 63–66.
(8) Lee, J. H.; Leu, I. C.; Hsu, M. C.; Chung, Y. W.; Hon, M. H. *J. Phys. Chem. B* **2005**, *109*, 13056–13059.
(9) (a) Shen, G. Z.; Bando, Y.; Ye, C. H.; Yuan, X. L.; Sekiguchi, T.; Golberg, D. *Angew. Chem., Int. Ed.* **2006**, *45*, 7568. (b) Hwang, J.; Min, B.; Lee, J. S.; Keem, K.; Cho, K.; Sung, M. Y.; Lee, M. S.; Kim, S. *Adv. Mater.* **2004**, *16*, 422–425.
(10) Fan, H. J.; Gösele, U.; Zacharias, M. *Small* **2007**, *3*, 1660–1671.
(11) Martin, C. R. *Science* **1994**, *266*, 1961–1966.
(12) Ajayan, P. M.; Stephan, O.; Redlich, Ph.; Colliex, C. *Nature* **1996**, *375*, 564–567.
(13) Yan, C. L.; Xue, D. F. *Adv. Mater.* **2008**, *20*, 1055–1058.
(14) Liu, Z.; Zhang, D.; Han, S.; Li, C.; Lei, B.; Lu, W.; Feng, J.; Zhou, C. *J. Am. Chem. Soc.* **2005**, *127*, 6–7.
(15) Fan, H. J.; Knez, M.; Scholz, R.; Nielsch, K.; Pippel, E.; Hesse, D.; Zacharias, M.; Gösele, U. *Nat. Mater.* **2006**, *5*, 627–631.

Published on Web 11/12/2009

the reactive template was excess, it was also necessary to etch away the remaining template.[10] In this paper, we present a new formation mechanism referred to as "sacrificial template-accelerated hydrolysis" (STAH) to create metal oxide nanotubes, using ion oxide as a case study. Typically, the concept involves acid-dissoluble metal oxide template and easy-hydrolyzed metal salt precursor; the possibility of selecting appropriate pairs of template and precursor renders this concept with tremendous flexibility and makes it potentially extendable to a wide variety of nanotube materials. Unlike previous reactive templates,[1,3] the template used in our study does not contribute to the component of final nanotubes, but can be in situ dissolved by the product of the precursor hydrolysis. Interestingly, the template dissolution in turn accelerates the hydrolysis, serving as a crucial step to initiate the nanotube formation.

Iron oxide is one of the most investigated nanomaterials for both biological and industrial applications. Hematite (α-Fe_2O_3), the most stable phase of iron oxide, has broad technological potential in gas sensors,[16,17] catalysis,[18] field emission,[19] magnetic storage,[20] and pigments. It is particularly a promising anode material (theoretical capacity: 1007 mA h g^{-1}) in lithium ion batteries (LIBs) that are expected to power future high efficiency plug-in hybrid electric vehicles.[17,21−26] Hematite is also the raw material for the synthesis of γ-Fe_2O_3 and Fe_3O_4. There has been considerable progress in the preparation of iron oxide controlled nanostructures in the powder form.[17,26−28] Hematite nanowires/rods and nanobelts as well as porous/tubular films were also grown from Fe foils through thermal oxidation or by anodization (severe corrosion),[19,29−31] on ITO,[32] or within AAO.[33] Nevertheless, there is still a big challenge to develop well-defined iron oxide nanotube arrays on large-area nonreactive solid substrates that possess persistent integrality throughout the tube growth, especially for LIB applications.

In this report, the rational synthesis of vertically aligned hematite nanotubes on bulk alloy substrate is achieved based on the STAH mechanism using ZnO nanowire array as the template. The reason we choose ZnO template is because of its structural versatility, easy synthesis and abundant availability;[34] but in principle any metal-oxide nanostructure can be applied so long as it is dissolvable by H^+. With a slight experimental variation, we can also obtain Fe_3O_4 nanotube arrays. In addition, with an introduction of glucose (a very abundant and inexpensive carbohydrate that can be economically produced from biomass) into the precursor solution, carbon/hematite (C/α-Fe_2O_3) nanotube arrays can also be obtained, with a large number of pores and uniform carbon distribution at a nanoscale in the walls. Such purposely designed composite nanostructures have an enhanced electronic conduction and physical buffering effect arising from the nanoscale hybrid of carbon with α-Fe_2O_3, as well as the hollow, porous and aligned architectures. Therefore, when employed directly as LIB anodes, these composite nanotubes exhibit exceptional capacity retention and outstanding rate capability.

2. Experimental Section

Synthesis of Nanotube Arrays. The ZnO nanowire arrays were grown on alloy substrate according to previous work.[35] For the fabrication of iron oxide nanotube arrays, the as-synthesized ZnO arrays were first placed into a 50 mL aqueous solution containing 0.27 g of $Fe(NO_3)_3 \cdot 9H_2O$ and kept still at room temperature for 10 h. We chose 10 h for immersion to ensure sufficient dissolution of ZnO. After the immersion, it was taken out, dried in air, and treated at 450 °C in Ar and H_2 for 5 h to obtain α-Fe_2O_3 and Fe_3O_4 nanotube arrays, respectively. The growth of iron oxide ill-oriented nanotube arrays (or random films) was achieved in the same way but using ZnO nanowires not vertically well-aligned (or distributed randomly) on the substrate surface. To grow C/α-Fe_2O_3 composite nanotube array, we used 50 mL of a homogeneously mixed solution of 0.23 g of glucose and 0.27 g o $fFe(NO_3)_3 \cdot 9H_2O$ for immersion, and the immersed-array was finally subjected to heat treatment in an Ar atmosphere at 450 °C for 24 h.

Characterization and Battery Test. Powder X-ray diffraction (XRD) (Bruker D-8 Avance), transmission electron microscopy (TEM) (JEM-2010FEF, 200 kV), scanning electron microscopy (SEM) (JSM-6700F, 5.0 kV), and Raman spectroscopy (Witech CRM200, 532 nm) were used to characterize the array products. Thermogravimetric analysis (TGA) was carried out on an SDT600 apparatus with a heating rate of 10 °C min^{-1} in N_2. The mass of electrode materials was measured on BS 124 S

(16) Hu, X. L.; Yu, J. C.; Gong, J. M.; Li, Q.; Li, G. S. *Adv. Mater.* **2007**, *19*, 2324–2329.
(17) Chen, J.; Xu, L.; Li, W.; Gou, X. *Adv. Mater.* **2005**, *17*, 582–586.
(18) Cesar, I.; Kay, A.; Gonzalez-Martinez, J. A.; Gratzel, M. *J. Am. Chem. Soc.* **2006**, *128*, 4582–4583.
(19) Yu, T.; Zhu, Y.; Xu, X.; Yeong, K.-S.; Shen, Z.; Chen, P.; Lim, C.-T.; Thong, J. T.-L.; Sow, C.-H. *Small* **2006**, *2*, 80–84.
(20) Zeng, H.; Li, J.; Liu, J. P.; Wang, Z. L.; Sun, S. H. *Nature* **2002**, *420*, 395–398.
(21) Poizot, P.; Laruelle, S.; Grugeon, S.; Dupont, L.; Tarascon, J. M. *Nature* **2000**, *407*, 496–499.
(22) Reddy, M. V.; Yu, T.; Sow, C. H.; Shen, Z. X.; Lim, C. T.; Rao, G. V. S.; Chowdari, B. V. R. *Adv. Funct. Mater.* **2007**, *17*, 2792–2799.
(23) Zhang, W.-M.; Wu, X.-L.; Hu, J.-S.; Guo, Y.-G.; Wan, L.-J. *Adv. Funct. Mater.* **2008**, *18*, 3941–3946.
(24) Li, J.; Dahn, H. M.; Krause, L. J.; Le, D.-B.; Dahn, J. R. *J. Electrochem. Soc.* **2008**, *155*, A812–A816.
(25) NuLi, Y.; Zhang, P.; Guo, Z. P.; Liu, H. K. *J. Electrochem. Soc.* **2008**, *155*, A196–A200.
(26) Wu, X. L.; Guo, Y. G.; Wan, L. J.; Hu, C. W. *J. Phys. Chem. C* **2008**, *112*, 16824–16829.
(27) Jia, C. J.; Sun, L. D.; Yan, Z. G.; You, L. P.; Luo, F.; Han, X. D.; Pang, Y. C.; Zhang, Z.; Yan, C. H. *Angew. Chem., Int. Ed.* **2005**, *44*, 4328–4333.
(28) Xiong, Y.; Li, Z.; Li, X.; Hu, B.; Xie, Y. *Inorg. Chem.* **2004**, *43*, 6540–6542.
(29) (a) Zhang, W. X.; Yang, S. H. *Acc. Chem. Res.* **2009**, *42*, 1617–1627. (b) Wen, X. G.; Wang, S.; Ding, H. Y.; Wang, Z. L.; Yang, S. H. *J. Phys. Chem. B* **2005**, *109*, 215–220.
(30) (a) LaTempa, T. J.; Feng, X. J.; Paulose, M.; Grimes, C. A. *J. Phys. Chem. C* **2009**, *113*, 16293–16298. (b) Prakasam, H. E.; Varghese, O. K.; Paulose, M.; Mor, G. K.; Grimes, C. A. *Nanotechnology* **2006**, *17*, 4285–4291.
(31) Mohapatra, S. K.; John, S. E.; Banerjee, S.; Misra, M. *Chem. Mater.* **2009**, *21*, 3048–3055.
(32) Vayssieres, L.; Sathe, C.; Butorin, S. M.; Shuh, D. K.; Nordgren, J.; Guo, J. H. *Adv. Mater.* **2005**, *17*, 2320–2323.
(33) Bachmann, J.; Jing, J.; Knez, M.; Barth, S.; Shen, H.; Mathur, S.; Gösele, U.; Nielsch, K. *J. Am. Chem. Soc.* **2007**, *129*, 9554–9555.
(34) Zeng, H. B.; Xu, X. J.; Bando, Y.; Gautam, U. K.; Zhai, T. Y.; Fang, X. S.; Liu, B. D.; Golberg, D. *Adv. Funct. Mater.* **2009**, *19*, 3165–3172.
(35) Liu, J. P.; Huang, X. T.; Li, Y. Y.; Ji, X. X.; Li, Z. K.; He, X.; Sun, F. L. *J. Phys. Chem. C* **2007**, *111*, 4990–4997.

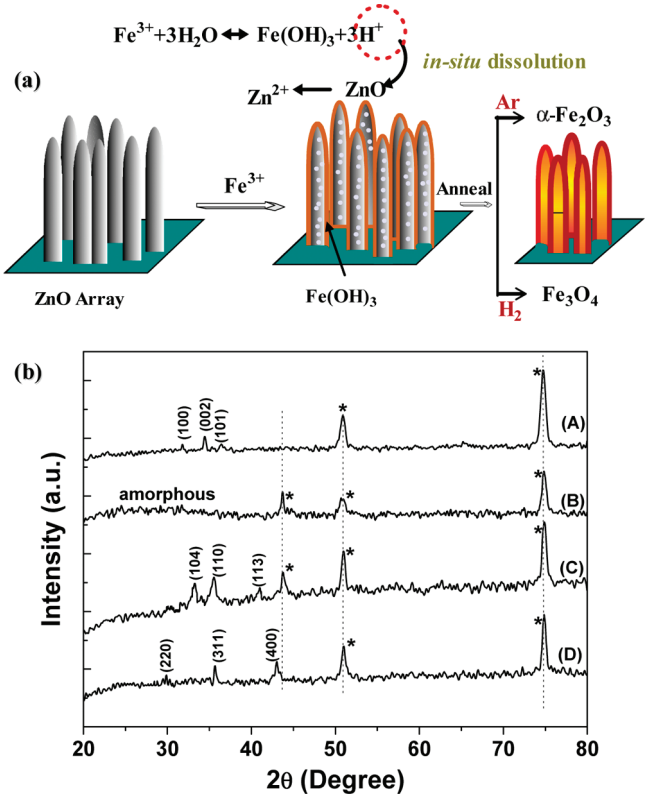

Figure 1. (a) Schematic diagram of the formation process of iron oxide nanotube arrays. (b) XRD patterns of ZnO nanowire array after the immersion in (A) Fe^{3+} solution for 30 min, (B) $Fe(OH)_3$ nanotube array, (C) α-Fe_2O_3 nanotube array, and (D) Fe_3O_4 nanotube array. Peaks marked with stars are from alloy substrate.

Balance (Max: 120 g; d = 0.1 mg). The Swagelok-type battery was assembled in an Ar-filled glovebox (Mbraun, Unilab, Germany) by directly using the C/α-Fe_2O_3 (or α-Fe_2O_3) nanotube array (0.82 mg or 0.74 mg) on alloy foil as the anode (13 mm diameter, array on one side of the foil was removed beforehand for electrical contacting), a Li-metal circular foil (0.59 mm thick) as the counter and reference electrodes, a microporous polypropylene membrane as the separator, and 1 M solution of $LiPF_6$ in ethylene carbonate (EC) and diethyl carbonate (DEC) (1:1 by volume) as the electrolyte. The cell was aged for 15 h before measurement. The discharge−charge cycling was performed at room temperature by using a multichannel battery tester (model SCN, USA).

3. Results and Discussion

3.1. Description of STAH. Figure 1a illustrates schematically our synthetic strategy for the design of iron oxide nanotube arrays. First, ZnO nanowire arrays are grown on bulk alloy substrates using a highly reliable, scalable, and economic solution process developed in our laboratory.[35,36] These ZnO nanowire arrays (see the Supporting Information, Figure S1a) are used as the starting template and immersed in an aqueous solution containing Fe^{3+} at room temperature. During the immersion, Fe^{3+} starts to hydrolyze, resulting in $Fe(OH)_3$ colloid and H^+. The hydrolysis occurs preferentially around the ZnO nanowires which also serves as a "patterned" substrate to support the $Fe(OH)_3$ colloids. Simultaneously, the ZnO nanowires are etched by H^+. This consumption of H^+ accelerates the reaction $Fe^{3+} + 3H_2O \rightarrow Fe(OH)_3 + 3H^+$, leading to an enhanced hydrolysis in the vicinity of the ZnO nanowires. As a result, the precipitation of $Fe(OH)_3$ emerges on the scaffold of ZnO nanowires, forming the early rigid base of nanotubes. Progressive hydrolysis and template dissolution eventually result in well-oriented $Fe(OH)_3$ nanotubes (see Figure S1b and c in the Supporting Information). On the basis of the proposed STAH mechanism, the ZnO nanowires have 2-fold functions: First, they are a removable/sacrificial template (i.e., neither Zn nor O was incorporated into the final product) for the formation of nanotubes; Second, the in situ dissolution exerts an acceleration effect on the hydroxide precipitation. It should be mentioned that the initial physical contact between ZnO and the alloy substrates is preserved after the transformation to $Fe(OH)_3$ nanotubes. This is essential for the lithium ion storage application, as a charge transport path should be maintained. This method provides a new principle for designing nanotubes, enabling well-oriented nanotube array fabrication on solid substrates without any porous membranes (AAO or polymers). The fabrication is easily achievable on a large area substrate (≥30 cm^2). Furthermore, it can be extended to iron oxide films with various morphologies simply by adopting the ZnO template, that is, it is a morphology-reservation transformation.

3.2. Iron Oxide Nanotubes. Evidence of the composition evolution is given by X-ray diffraction (XRD). After immersion in Fe^{3+} solution for 30 min, it is observed from XRD patterns that the crystallinity of ZnO nanowires was lowered and their orientation relative to alloy substrate was reduced gradually (Figure 1b(A)). The peaks labeled with stars come from the alloy foil.[37] With the immersion time prolonged, ZnO peaks disappeared completely at the end and only a broad peak relating to amorphous $Fe(OH)_3$ could be found (Figure 1b(B)). The formation of $Fe(OH)_3$ was further confirmed by thermogravimetric (TGA) analysis, from which ~26.2% weight loss was observed (Figure S1d in the Supporting Information; expected weight loss from $Fe(OH)_3$ to Fe_2O_3 is 25.23%). After this stage, the resulting $Fe(OH)_3$ nanotube arrays were calcinated in Ar at 450 °C and transformed into ordered arrays of α-Fe_2O_3 nanotubes, as evidenced from XRD (Figure 1b(C), JCPDS 33−0664). Raman spectrum (Figure 2a) also demonstrates the pure phase of α-Fe_2O_3.[19] EDS compositional analysis (not shown here) shows no Zn signal, indicating the complete consumption of the ZnO template.

Images b and c in Figure 2 display representative scanning electron microscopy (SEM) images of the well-defined nanotube arrays. The columnar nanotubes have closed tips and are assembled from numerous nanoparticles, with outer diameters ranging from 200 to 300 nm.

(36) Liu, J. P.; Li, Y. Y.; Ding, R. M.; Jiang, J.; Hu, Y. Y.; Ji, X. X.; Chi, Q. B.; Zhu, Z. H.; Huang, X. T. *J. Phys. Chem. C* **2009**, *113*, 5336–5339.

(37) Liu, J. P.; Li, Y. Y.; Huang, X. T.; Li, G. Y.; Li, Z. K. *Adv. Funct. Mater.* **2008**, *18*, 1448–1458.

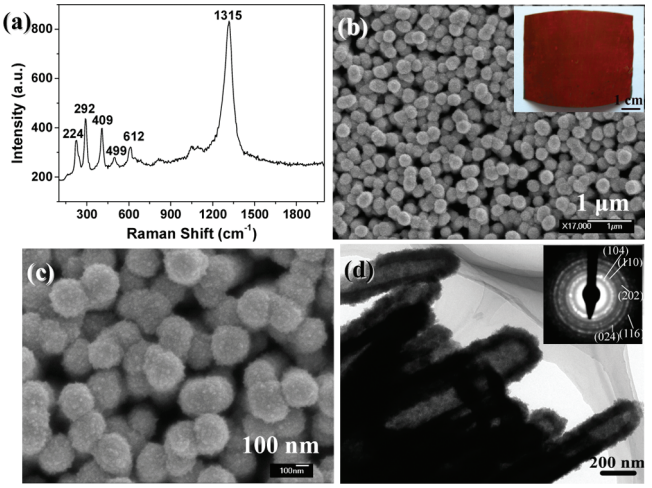

Figure 2. (a) Raman spectrum of α-Fe_2O_3 nanotube array. (b) Low-magnification and (c) enlarged SEM images of the array. Inset in b is a typical optical image of the array on a large-area alloy substrate. (d) TEM image and SAED pattern of several α-Fe_2O_3 nanotubes.

As shown in the inset of Figure 2b, the arrays can grow uniformly on an alloy substrate as large as ~30 cm^2, while maintaining a robust mechanical adhesion even with bending. More evidence on the composition and structure of the product is given by transmission electron microscopy (TEM) analysis. Tubular structures consisting of nanogranular walls can be seen in Figure 2d, consistent with the SEM result. The selected-area electron diffraction (SAED) pattern (inset of Figure 2d) reveals the polycrystalline hematite composition of these tubes.

When a reduction of the as-obtained samples by H_2 at 450 °C was conducted, the $Fe(OH)_3$ nanotubes were converted to Fe_3O_4 arrays, accompanied by a color change from red brown to black. Although the morphology is similar to the α-Fe_2O_3 nanotube array, XRD (Figure 1b(D), JCPDS 65−3107) gives clear evidence of the Fe_3O_4 phase.

As a demonstration of the shape-preservation transformation characteristic of the present STAH process, other forms of ZnO nanowire templates were also used. Figure S2a−d (see the Supporting Information) show the results using less-oriented ZnO arrays and even disordered ZnO nanowires to fabricate various iron oxide films. The morphology of the nanowire template is translated to the final nanostructure with a high level of control. Although we only demonstrate here the fabrication of α-Fe_2O_3 nanotube arrays on alloy substrate because of our intention to use them directly in electrochemistry devices, it is also possible to obtain such regularly oriented tubular arrays on many other substrates such as ITO and ceramics for desirable applications. Figure S2e in the Supporting Information illustrates the similar α-Fe_2O_3 growth on commercial ceramic substrate.

3.3. Carbon/α-Fe_2O_3 Composite Nanotubes. The STAH mechanism can be utilized to generate iron oxide-based composite nanotube arrays. As an example, arrays of C/α-Fe_2O_3 nanotubes are successfully obtained following the same approach but adding glucose into the Fe^{3+} solution for immersion. The synthesized arrays also demonstrate a uniform coverage on the alloy substrate

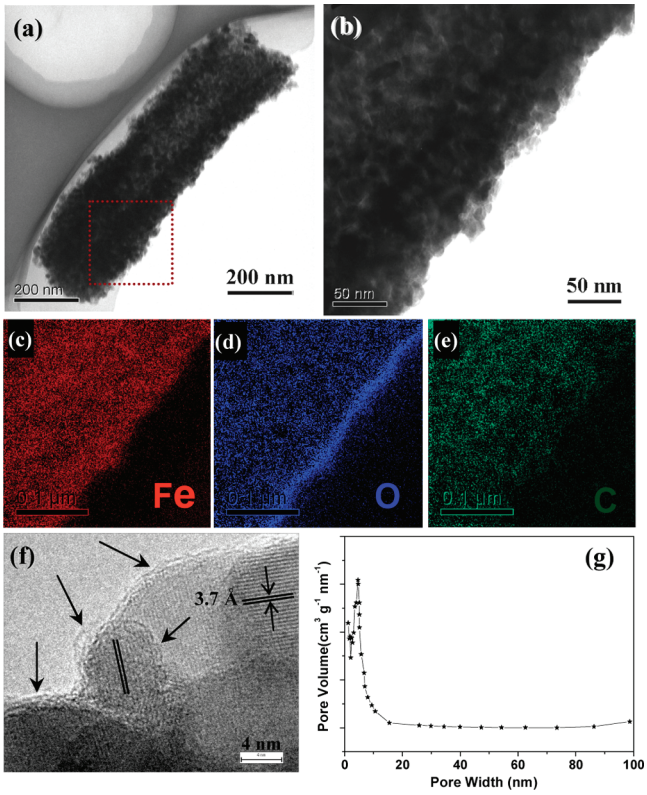

Figure 3. (a, b) Single C/α-Fe_2O_3 nanotube. (c−e) EELS elemental mapping results. (f) HRTEM image of the C/α-Fe_2O_3 nanotube. Arrows indicate the carbon layers. (g) Pore size distribution of C/α-Fe_2O_3 nanotubes.

(see the Supporting Information, Figure S3a,b). Figure 3a shows the TEM micrograph of an individual C/α-Fe_2O_3 nanotube of ~200 nm diameter. Again, the tube walls are assembled from nanoparticles. Part of the tube-wall near the closed end (the rectangular area) is further enlarged in Figure 3b. The compositions of this part are studied by the electron energy loss spectroscope (EELS) elemental mapping (Figure 3c−e). As can be seen, the homogeneous existence of Fe, O, and carbon in the nanotube wall is unambiguously illustrated. Within the tube wall, a lattice spacing of ~0.37 nm for (012) planes of α-Fe_2O_3 is resolved in the high-resolution TEM image (HRTEM, Figure 3f and the Supporting Information, Figure S3c). In particular, thin carbon layers of average 1.5 nm in thickness are coated tightly on the surface of most α-Fe_2O_3 nanoparticles (indicated by arrows in Figure 3f). This result further confirms the nanoscale carbon hybridization, in agreement with the EELS observation. The carbon content is determined to be ~10.7% by thermogravimetric analysis (TGA). The emergence of carbon stems from the initial adsorption of high-affinity glucose[36] into colloid $Fe(OH)_3$ during the immersion and the subsequent carbonization of glucose upon calcination. Pore size distribution measurement (Figure 3g) reveals that the composite nanotubes have average pore size of 4 nm in the structure, the consequence of dehydration of $Fe(OH)_3$ and crystallization of amorphous Fe_2O_3.

3.4. Lithium-Ion Storage Properties. The C/α-Fe_2O_3 nanotube arrays with a physical adhesion to conductive

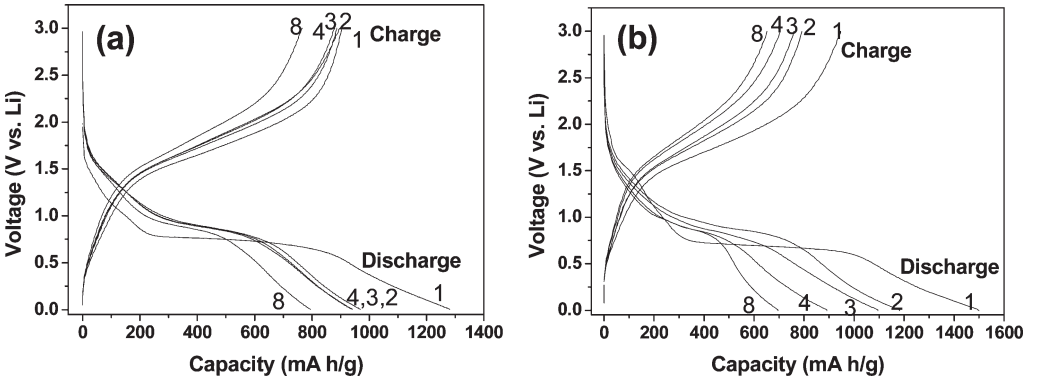

Figure 4. Voltage−capacity traces of (a) C/α-Fe_2O_3 and (b) pristine α-Fe_2O_3 nanotube arrays.

substrates fulfill the key requirements for LIB electrode materials (viz., electronic conductivity, porosity for ion diffusion, uniformity, and mechanical robustness). Therefore, they can be directly used as a potential polymer binder-free substitute for current graphite LIB anodes. Such array was electrochemically evaluated versus Li under galvanostatic condition (*C*/5, 1*C* was defined as 4 Li^+/h; 671 mA g^{-1}) in the potential window of 0.005−3 V (Figure 4a). The voltage-capacity trace of pristine α-Fe_2O_3 nanotube array was also recorded for comparison (Figure 4b). The electrochemical behavior of the two electrodes are similar and in general consistency with the literature.[25,26] In the first discharge curve of C/α-Fe_2O_3, a poorly defined plateau (1.6−0.8 V) and a perfect one at 0.75 V are clearly observed. The first plateau can be ascribed to the formation of cubic $Li_2Fe_2O_3$, and the second could be attributed to the reduction from Fe^{2+} to Fe^0 and the formation of amorphous Li_2O.[22,26] In agreement with this result, two reduction peaks (∼1.5 and 0.71 V) are identified in the differential capacity versus voltage plot (inset in Figure 5a). A broad oxidation peak centered at 1.74 V is also present, corresponding to the reversible oxidation of Fe^0 to Fe^{3+} during the charge process.[25] Since carbon itself has a small capacity of ∼372 mA h g^{-1}, the presence of carbon lowers the first discharge capacity of C/α-Fe_2O_3 nanotube array. The distinct difference between C/α-Fe_2O_3 and α-Fe_2O_3 nanotube array electrodes is demonstrated from cycling performance up to 150 cycles, as shown in Figure 5a. It is evident that the C/α-Fe_2O_3 electrode exhibits exceptional cyclability; even though the capacity decays gradually in the first 20 cycles, it stabilizes around 700 mA h g^{-1} in the following 60 cycles. After 150 cycles, the electrode still delivers a reversible capacity of as high as 659 mA h g^{-1}, with a fading rate of only ∼0.586 mAh g^{-1} per cycle during the last 70 cycles. In contrast, the capacity of the pristine α-Fe_2O_3 electrode decreases continuously and only 384 mA h g^{-1} can be retained at the end.

The C/α-Fe_2O_3 nanotube array electrode shows a long cycle life while still exhibiting a relatively high capacity even at high current rates. As illustrated in Figure 5b, it retains reversible capacities of 523 and 463 mA h g^{-1} after 50 and 150 cycles at 1.5*C*, respectively. At a higher rate of 3*C*, capacities of 457 mA h g^{-1} can be achieved after

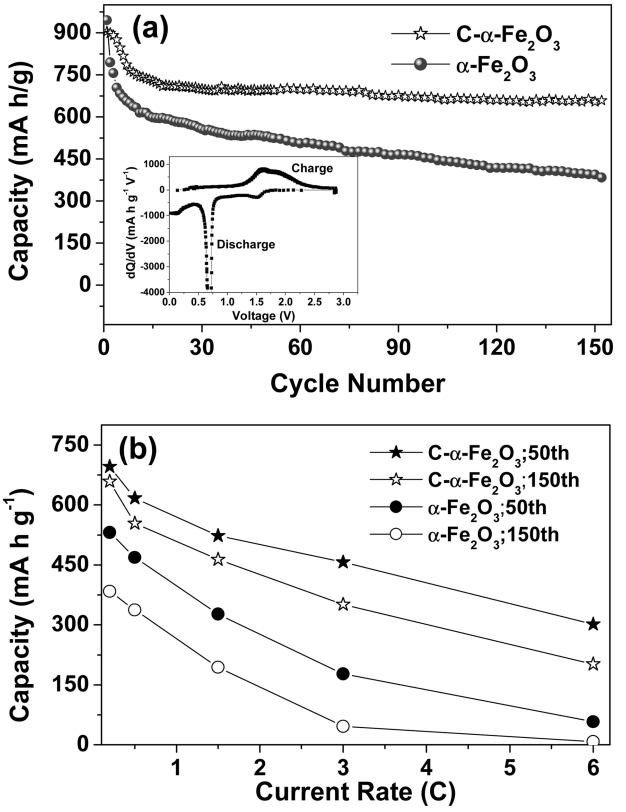

Figure 5. (a) Cycling performance at the *C*/5 rate for α-Fe_2O_3 and *C*/α-Fe_2O_3 nanotube arrays. Inset is the first-cycle differential capacity versus voltage plot of *C*/α-Fe_2O_3. (b) Charge capacity versus current rate plots of α-Fe_2O_3 and *C*/α-Fe_2O_3 nanotube arrays.

50 cycles and 351 mA h g^{-1} can be retained after the 150th cycling. The later value is still comparable to that of commercial graphite. Even at 6*C* (4026 mA g^{-1}), the C/α-Fe_2O_3 electrode delivers a reversible capacity of 301 mA h g^{-1} up to the 50th cycle. As for the α-Fe_2O_3 nanotubes, increasing the rate to 1.5*C* leads to capacities of only 327 and 193 mA h g^{-1} after 50 and 150 cycles, respectively (Figure 5b). At a 6*C* rate, nearly no capacity can be retained at the end of the test, in distinct contrast to C/α-Fe_2O_3.

For a better understanding of the advantage of C/α-Fe_2O_3 nanotubes array in lithium energy storage, the cycling response at continuously variable rates was evaluated (Figure 6). When the electrode is first cycled at a rate as high as 12*C* (8052 mA g^{-1}), it can retain a capacity

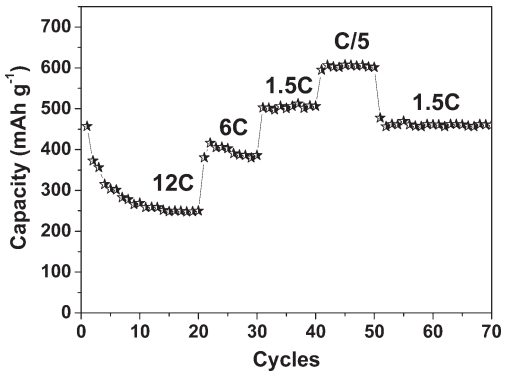

Figure 6. Cycling stability at various *C* rates for C/α-Fe_2O_3 nanotube arrays.

of ~250 mA h g^{-1} even after 20 cycles. Subsequently, the rate is decreased stepwise to *C*/5, with a pronounced increase in the capacity. As can be seen, the electrode delivers stable capacities of 500 and 605 mA h g^{-1} at 1.5*C* and *C*/5, respectively. After 50 cycles, with the current rate being again increased back to 1.5*C*, a capacity of 460 mA h g^{-1} can be recovered; this value lasts up to the 70th cycle without any loss.

Considering that no traditional carbon black and polymer binders were used in the present work, the reversible capacity and cyclability presented above for C/α-Fe_2O_3 are highly encouraging. Our C/α-Fe_2O_3 nanotubes comprise numerous nanoparticle subunits, which are α-Fe_2O_3 particles encapsulated within thin carbon shells. Every shell is tightly attached to α-Fe_2O_3, favorable for mechanical reinforcement and electrical conductivity enhancement.[38−42] Herein, we emphasize the beneficial nanosize effects: At a scale smaller than 20 nm, the volume change of α-Fe_2O_3 upon Li uptake and removal can be minimized more efficiently by the mechanical buffering of the carbon shell. In the meantime, the carbon coating around every α-Fe_2O_3 nanoparticle also ensures the electrical contact throughout the whole nanotube body during the cycling. This explains why the C/α-Fe_2O_3 nanotube array electrode has superior performance over the pristine α-Fe_2O_3 array electrode. It is noteworthy that our case is quite different from the literature; in the latter case, carbon was typically coated on the outline of the overall nanostructures[23,36,43−45] or used for nanostructures loading.[46] Without carbon, α-Fe_2O_3 nanotubes have a poor inherency so that the electrical continuity and structural integrity during cycling, especially at high rates, may not be maintained.

Nevertheless, it should be noted that the cycling stability of the pristine α-Fe_2O_3 nanotubes array in our case is still enhanced when compared to other α-Fe_2O_3 nanostructures, for which the capacities faded rapidly to lower than 50% of the initial values after only 40 cycles even at low rates.[25,26] We propose several reasons for this: First, the porous nature of nanosized tube walls allows a fast Li-ion diffusion. Meanwhile, the hollow space of nanotubes offers better electrolyte accessibility and can accommodate a larger degree of structural deformation due to volume variation during Li insertion/extraction. Second, the high porosity of the tubewalls provides larger material-electrolyte contact areas, rendering an increased number of electrochemically active surface sites. Finally, the direct and good alignment of nanotubes on conductive substrates ensures continuous pathways for electron transports.[36,37,47−51]

4. Conclusions

In summary, a novel facile and inexpensive STAH strategy has been developed for the first time to fabricate inorganic nanotubes. Using ZnO nanowire arrays as templates, we have demonstrated that nanotube arrays of iron oxide-based nanostructures including pristine α-Fe_2O_3, Fe_3O_4, and C/α-Fe_2O_3, as well as random films of these materials can be achieved on large-area conductive metal substrates. Our strategy is extendable to many other reaction systems involving dissolvable templates in acids and easily hydrolyzed metal salt precursors. In particular, it opens new avenues for rational design of optimal composite electrode materials for high-performance LIBs. The C/α-Fe_2O_3 composite nanotube array, as a model example, has manifested excellent cyclability and high rate capability, attributed to the nanoscale intimate contact of α-Fe_2O_3 with conductive carbon framework and the unique porous tubular nanostructures readily derived from STAH. The regular array of C/α-Fe_2O_3 nanotubes may also find application potentials as catalysis and chemical sensors. Because low mass of active electrode material leads to very limited energy per unit surface area, our future work will focus on using nanowire templates with higher aspect ratio to produce nanotubes with more mass on electrode substrates.

Acknowledgment. The authors appreciate the financial support from the National Natural Science Foundation of China (50872039; 50802032). The authors also thank Prof. J. B. Wang at Wuhan University for his kind assistance in the EELS measurement.

Supporting Information Available: SEM images of ZnO nanowire array template and $Fe(OH)_3$ nanotube arrays. TG and DTA traces of the immersed product ($Fe(OH)_3$). SEM images of various α-Fe_2O_3 films. SEM images and HRTEM image of C/α-Fe_2O_3 nanotubes (PDF). This material is available free of charge via the Internet at http://pubs.acs.org.

(38) Derrien, G.; Hassoun, J.; Panero, S.; Scrosati, B. *Adv. Mater.* **2007**, *19*, 2336–2340.
(39) Ng, S. H.; Wang, J. Z.; Wexler, D.; Konstantinov, K.; Guo, Z. P.; Liu, H. K. *Angew. Chem., Int. Ed.* **2006**, *45*, 6896–6899.
(40) Kim, H.; Cho, J. *Nano Lett.* **2008**, *8*, 3688–3691.
(41) Cui, G. L.; Hu, Y. S.; Zhi, L. J.; Wu, D. Q.; Lieberwirth, I.; Maier, J.; Müllen, K. A *Small* **2007**, *3*, 2066–2069.
(42) Kwon, Y.; Cho, J. *Chem. Commu.* **2008**, 1109–1111.
(43) Wang, Y.; Zeng, H. C.; Lee, J. Y. *Adv. Mater.* **2006**, *18*, 645–649.
(44) Lou, X. W.; Li, C. M.; Archer, L. A. *Adv. Mater.* **2009**, *21*, 2536–2539.
(45) Zhang, W. M.; Hu, J. S.; Guo, Y. G.; Zheng, S. F.; Zhong, L. S.; Song, W. G.; Wan, L. *J. Adv. Mater.* **2008**, *20*, 1160–1165.
(46) Zhang, H. X.; Feng, C.; Zhai, Y. C.; Jiang, K. L.; Li, Q. Q.; Fan, S. S. *Adv. Mater.* **2009**, *21*, 2299–2304.
(47) Taberna, P. L.; Mitra, S.; Poizot, P.; Simon, P.; Tarascon, J. M. *Nat. Mater.* **2006**, *5*, 567–573.
(48) Li, Y.; Tan, B.; Wu, Y. *Nano. Lett.* **2008**, *8*, 265–270.
(49) Chan, C. K.; Peng, H.; Liu, G.; McIlwrath, K.; Zhang, X. F.; Huggins, R. A.; Cui, Y. *Nat. Nanotechnol.* **2008**, *3*, 31–35.
(50) Liu, J. P.; Li, Y. Y.; Huang, X. T.; Ding, R. M.; Hu, Y. Y.; Jiang, J.; Liao, L. *J. Mater. Chem.* **2009**, *19*, 1859–1864.
(51) Xiao, W.; Chen, J. S.; Li, C. M.; Xu, R.; Lou, X. W. *Chem. Mater.* **2009**No. DOI: 10.1021/cm9012014.